Fuel 227 (2018) 379–385

Contents lists available at ScienceDirect

Fuel

journal homepage: www.elsevier.com/locate/fuel

Full Length Article

Chemo-morphological coupling during serpentine heat treatment for carbon mineralization

Meishen Liu, Greeshma Gadikota*

Department of Civil and Environmental Engineering, Environmental Chemistry and Technology Program, Geological Engineering Program, Grainger Institute for Engineering, University of Wisconsin-Madison, Madison, WI 53706, United States

ARTICLE INFO

Keywords:
Serpentine
Heat treatment
X-ray scattering
Morphology
Crystal structure

ABSTRACT

One of the safest and permanent routes for potentially capturing and storing CO_2 is via carbon mineralization which involves converting CO_2 into environmentally benign and thermodynamically stable calcium and magnesium carbonates. One of the most abundant Mg-bearing minerals in the world suitable for carbon mineralization is serpentine ($Mg_3Si_2O_5(OH)_4$). To enhance the reactivity of serpentine with CO_2, dehydroxylation by heating to temperatures in the range of 600 °C–700 °C was proposed. To establish a fundamental structural and morphological basis for the enhanced reactivity of serpentine (e.g. lizardite) on heating to temperatures in this range, *in-operando* synchrotron multi-scale X-ray scattering measurements were performed, with complementary analyses of the changes in the porosity, particle size, and surface morphology. The detailed transformation of lamellar serpentine to a pseudo-amorphous state on heating to temperatures in the range of 600 °C–700 °C, and the subsequent conversion to denser crystalline phases such as $Al_{2.35}Si_{0.64}O_{4.82}$ (mullite), SiO_2 (cristobalite), Mg_2SiO_4 (forsterite), and $Fe_{0.3}Mg_{0.7}(SiO_3)$ (enstatite) was determined from the wide and small angle X-ray scattering measurements. Increasing roughness of the pore-solid interface on heating to 700 °C followed by enhanced smoothness due to the formation of crystalline phases at higher temperatures was established from the combined ultra small and small angle X-ray scattering measurements. The transformation of lamellar lizardite to its pseudo-amorphous state corresponded to an increase in the porosity and surface area, while the formation of crystalline phases reduced the porosity and surface area while increasing the particle size.

1. Introduction

One of the challenges at the forefront of sustainable energy production is the safe and permanent capture and storage of CO_2 with potential for utilization One option is to capture and convert CO_2 into calcium and magnesium carbonates using earth-abundant calcium and magnesium-bearing silicates as the sources of alkalinity [1–9]. Serpentine ($Mg_3Si_2O_5(OH)_4$) is one example of an earth-abundant hydrated magnesium silicate mineral that has been extensively studied for carbon mineralization [2,4,10–15]. Various routes for serpentine carbonation have been explored including the conversion of CO_2 and serpentine into magnesium carbonate via direct gas-liquid-solid routes [2], or accelerated extraction of Mg followed by magnesium carbonate precipitation [4,13].

To accelerate the kinetics of CO_2 conversion to magnesium carbonate, the thermal activation of serpentine was proposed. Thermal activation of serpentine to temperatures up to 700 °C dehydroxylates the crystal lattice resulting in a more reactive amorphous material [16]. Previous studies reported carbonate conversions of heat-treated serpentine as high as 73.5% at 185 °C, P_{CO2} of 150 atm in 1.0 M NaCl + 0.64 M $NaHCO_3$ on reaction for 1 h [17]. More recent studies reported using flue gas concentrations for successfully converting heat-treated serpentine to magnesium carbonate [11,18]. Despite significant research efforts directed towards converting heat-treated serpentine to magnesium carbonate, there is a limited fundamental understanding of the structural and morphological changes that occur in serpentine on heating and the influence of these changes on the reactivity of the mineral.

While McKelvy and co-workers evaluated the changes in the structure of heat-treated serpentine using X-ray diffraction (XRD) and fourier transform infrared spectroscopy (FTIR) analyses [19], the corresponding morphological changes such as the porosity, pore-solid interfacial structure, and the surface area were not reported. Recent advances in synchrotron radiation have now allowed us to probe the changes in the morphologies and structures of porous materials from the angstrom to the micrometer-scale using ultra small, small, and wide angle X-ray scattering (USAXS/SAXS/WAXS) measurements [20–23]. In the case of serpentine, the changes in the lamellar structure and the

* Corresponding author.
E-mail address: gadikota@wisc.edu (G. Gadikota).

https://doi.org/10.1016/j.fuel.2018.04.097
Received 11 March 2018; Received in revised form 15 April 2018; Accepted 18 April 2018

Table 1
Composition of lizardite.

Components	Weight%	Components	Weight%
MgO	37.00	MnO	0.10
CaO	0.42	Na_2O	0.04
Fe_2O_3	8.09	K_2O	< 0.01
SiO_2	38.90	TiO_2	0.04
Cr_2O_3	0.40	P_2O_5	< 0.01
Al_2O_3	1.79	V_2O_5	0.02
		LOI%	13.20

interlayer basal spacing [24] were determined using wide angle X-ray scattering (WAXS) and small angle X-ray scattering (SAXS) measurements. Ultra small angle X-ray scattering (USAXS) measurements in conjunction with Brunauer–Emmett–Teller (BET) porosity measurements and particle size analyses were used to determine the morphological changes in serpentine on thermal treatment.

2. Experimental methods

The serpentine morph used in this study was lizardite. The chemical composition of the unreacted lizardite listed in Table 1 was determined using Wavelength Dispersion X-ray Fluorescence (WD-XRF, Pananalytical Axios, The Netherlands). The mean particle size, surface area and cumulative pore volume of the ground unreacted serpentine were found to be 10.80 μm, 36.3 m^2/g and 0.115 ml/g, respectively. In addition to lizardite, the other major phase present was identified as quartz (Fig. S1).

2.1. Heat treatment of serpentine

To determine the *in-operando* structural and morphological changes in serpentine on heat treatment, USAXS/SAXS/WAXS measurements were performed at Sector 9-ID at Advanced Photon Source (APS) in Argonne National Laboratory (ANL), Argonne, IL. Lizardite was prepared by grinding the material to a size smaller than 100 μm followed by compaction into pellets. The thickness of the pellet used in this experiment was 1 mm (± 0.2 mm). The heat treatment of the lizardite-bearing serpentine was performed by placing the pellet in a Linkam TS1500 heating stage (Linkam Scientific Instruments Ltd., Tadworth, UK) with temperature control of ± 0.1 °C. The temperature ramp rate was set at 3.3 °C/min and the temperature range was from 30 °C to 1150 °C. The heater was then aligned with the USAXS/SAXS/WAXS instrument at Sector 9-ID.

The USAXS/SAXS instruments are based on the original Bonse-Hart double-crystal configuration, which used multiple dispersive reflections from perfect crystals to reach a region of scattering vector q, where $q = (4\pi/\lambda)\sin\theta$, λ is the wavelength of the X-ray, and 2θ is the scattering angle [25,26]. All measurements (USAXS/SAXS/WAXS) could be made within about 3 min, reducing uncertainties bringing by the change of sample configuration within the beam [26]. The total X-ray flux of the measurement was 10^{-13} photon s^{-1}. The wavelength of the X-ray used in the experiment was 0.59 Å, which corresponded to the energy of 21.0 keV. Calibrations were made using silver behenate and the NIST standard reference material, SRM 640d (Si). Collected data were reduced and analyzed by the Irena and Nika software packages embedded in IgorPro (Wavemetrics, Lake Oswego, OR) [26–28].

Several complementary measurements were performed to complement the scattering measurements. Powdered lizardite was thermally treated to 350 °C, 650 °C, 900 °C, and 1150 °C in an oven for 3 h for determining the changes in the porosity, surface area, surface morphology and particle size on heating. The changes in the porosity and the specific surface area of the powdered lizardite on heating were determined using the BET technique (Quantachrome Autosorb1 Analyzer), while particle size distributions were determined via a laser diffraction method (Beckman Coulter, Inc., LS 13 320 MW). The surface morphological features were determined using a scanning electron microscopy (SEM, Hitachi High Technologies America, Hitachi S3400-N). The changes in the weight of the sample on heating was determined using thermogravimetric analysis (TGA, TA Instruments TGA550).

3. Results and discussion

3.1. Structural changes in lizardite on thermal treatment

Heating lamellar structures such as lizardite produced several changes across the material hierarchy. One of the characteristic features of hierarchical materials is the interlayer basal spacing which was observed in the SAXS regime. The interlayer space is the distance between the silicate layers in case of lizardite. One measure of the interlayer space is the basal reflection or the d (0 0 1) peak corresponding to the scattering from one hydrated magnesium silicate nanosheet and the interlayer space. The position and the intensity of the characteristic interlayer peak indicate the distance corresponding to the interlayer space and the nanosheet, and the quantity of interlayer nanopores, respectively. The interlayer basal reflection is a characteristic of other hierarchical natural materials such as clays [29,30].

In swelling clays such as Na- or Ca-montmorillonite, the interlayer basal spacing changes with the layers of intercalated water in these regions [21,26,27], unlike in non-swelling clays such as kaolinite [22]. In swelling clays bearing intercalated water, a reduction in the interlayer basal spacing is noted on heating to 150 °C [21,26,27]. Unlike swelling clays, phyllosilicates such as lizardite do not contain intercalated water. On heating to 150 °C, no significant changes in the positions of the d (0 0 1) or d (0 0 2) peaks or their intensities were noted (Figs. 1 and S2). This observation is attributed to the absence of the characteristic ability to shrink or swell due to the loss or gain of water, and no structural changes in the hydrated magnesium silicate nanosheet (see Fig. S3 which represents d (2 0 2) reflection in lizardite).

Further heating above 550 °C reduced the intensity of the interlayer basal reflection with the peak disappearing on heating to 825 °C. This observation is consistent with previous studies reporting changes in the lamellar structure of lizardite to an amorphous form due to the removal of –OH groups [16,19,31]. Thermogravimetric analyses of untreated lizardite showed the onset of weight loss around 500 °C with near complete loss achieved on heating to 825 °C which corresponds to lizardite dehydroxylation (Fig. 2). Various lizardite samples were also heat-treated at 350 °C, 650 °C and 900 °C in an *ex-situ* environment prior to thermogravimetric analyses. Heat treatment of lizardite at 350 °C did not change the weight of the sample significantly compared to the untreated serpentine. On heating to 650 °C, a weight loss of 2.25% was observed suggesting the presence of residual –OH groups. No significant changes in the weight of the sample were noted on heating to 900 °C suggesting the complete removal of –OH groups at those conditions. The observations of the changes in the weight of serpentine due to dehydroxylation in Fig. 2 are consistent with the loss in the crystalline structure of serpentine noted in Figs. 1, S2 and S3. In the context of carbon mineralization, the structural disorder achieved due to serpentine dehydroxylation on heating to temperatures in the range of 600 °C–700 °C was noted as a factor in accelerating carbon mineralization behavior [19].

On heating serpentine beyond 650 °C, the recrystallization of amorphous serpentine to denser phases was observed. The onset of $Al_{2.35}Si_{0.64}O_{4.82}$ (mullite), SiO_2 (cristobalite), Mg_2SiO_4 (forsterite), and $Fe_{0.3}Mg_{0.7}(SiO_3)$ (enstatite) phases was observed in the range of 700 °C–800 °C in the WAXS regime [32–35]. These observations are consistent with previous studies that reported a strong exotherm at 782 °C indicating the onset of new phase formation [19]. The intensity of these phases increased on further heating suggesting the growth of these phases (Fig. 3). These phases are indexed in serpentine heat-treated at 1150 °C (Fig. S4). The respective densities of mullite,

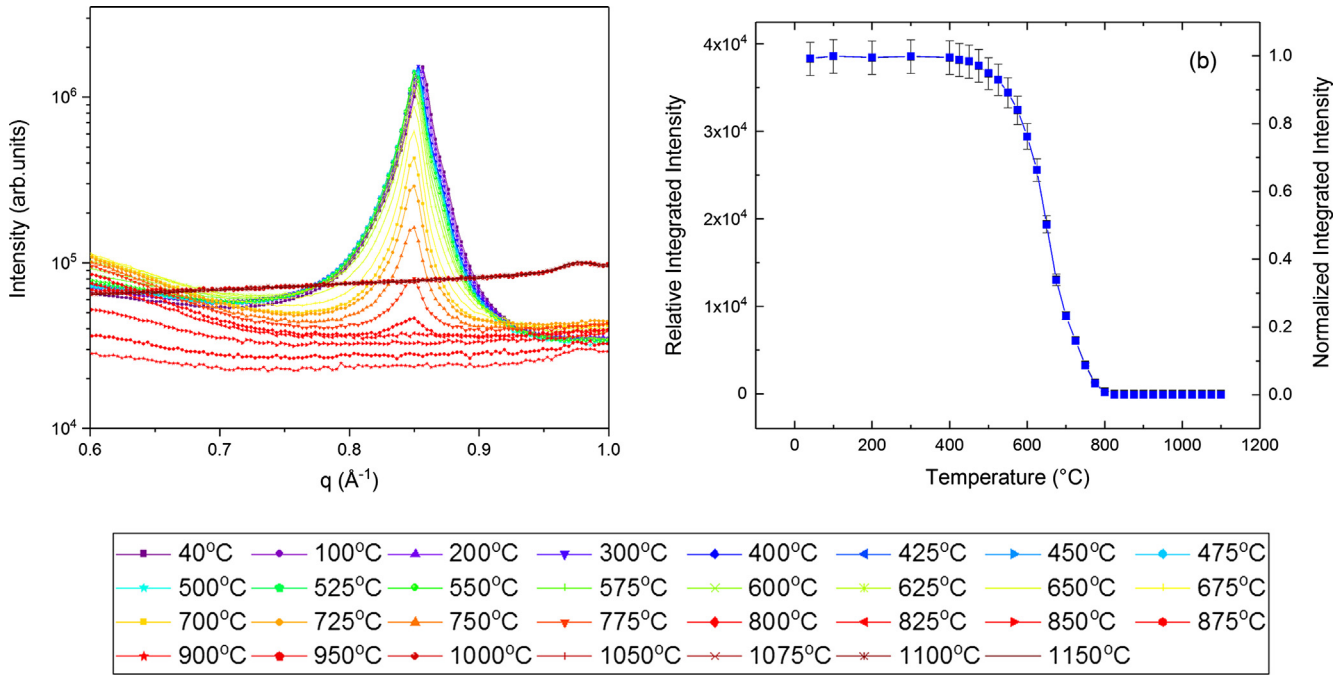

Fig. 1. Changes in (a) the characteristic lizardite peak (q = 0.85 Å^{-1}, d = 7.39 Å, hkl: (001)[42]) and (b) the integrated peak intensity on heating to 1150 °C. The relative integrated intensity represented in (b) is the integrated intensity of the characteristic lizardite peak at a given temperature normalized to the integrated intensity at 40 °C. Vertical bars in (b) represent estimated 5% standard deviation uncertainties.

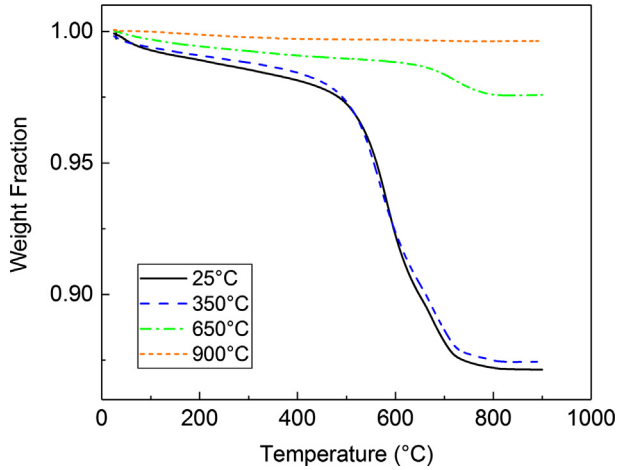

Fig. 2. Changes in the weight of lizardite heat-treated to 350 °C, 650 °C, and 900 °C with respect to untreated lizardite at 25 °C determined using thermogravimetric analysis.

cristobalite, forsterite, and enstatite are 3.15, 2.3, 3.3, and 3.3 g/cm^3 compared to the density of lizardite of 2.6 g/cm^3 [36–40]. To determine if less dense phases may have a more significant impact on mineralization compared to more dense phases, the corresponding morphological changes in lizardite on heat treatment were determined.

3.2. Morphological changes in lizardite on thermal treatment

In the previous section, the structural basis for high conversions of heat-treated serpentine to magnesium carbonate was established with reasonable agreement with published data [19]. However, there is a limited understanding of the corresponding morphological changes in lizardite on heat treatment and how that may potentially impact carbon mineralization behavior. To develop the morphological perspective, the changes in the particle size, porosity, surface area, and changes in the pore-solid interface on heating were evaluated. To evaluate the changes in the particle size, porosity, and surface area, lizardite was heat-treated to 350 °C, 650 °C, 900 °C, and 1150 °C.

One of the hypotheses to explain the enhanced reactivity of lizardite heat-treated to 650 °C is the potential increase in the porosity which aids the diffusion of Mg or Si ions into the bulk solution, thereby enhancing the carbonation potential. To test this hypothesis, BET measurements were performed at 25 °C, 350 °C, 650 °C and 900 °C. The cumulative pore volume increased from 0.115 cm^3/g to 0.888 cm^3/g and 1.563 cm^3/g on heating to 350 °C and 650 °C, respectively. The increase in cumulative pore volume corresponds to lizardite dehydroxylation. Heating to 900 °C reduced the cumulative pore volume to 0.047 cm^3/g (Table 2 and Fig. 4). The reduction in porosity at 900 °C is consistent with the formation of denser phases (Fig. 3). Similarly, an increase in the surface area was noted on the dehydroxylation of lizardite. The surface area increased from 36.3 m^2/g to 580.4 m^2/g and 1152 m^2/g at 350 °C and 650 °C, respectively. Further heating to 900 °C reduced the surface area to 6.5 m^2/g which corresponds to the growth of denser phases (Table 2). These data support the hypothesis that increase in porosity and surface area on heating to 650 °C along with the structural disorder noted in Section 3.1 aids the high reactivity of lizardite with CO_2 at this temperature.

To probe the factors leading to the changes in the porosity particularly on heating from 650 °C to 900 °C, the particle sizes of the serpentine heat-treated at various temperatures were determined. The particle size of the unreacted lizardite was in the range of 0.5 μm–50 μm. On heating to 350 °C and 650 °C, a small increase in the particle size from 10.8 μm at ambient temperature to 12.4 μm and 13.1 μm was noted (Table 2 and Fig. 5). On further heating to 900 °C, the volume of particles larger than 50 μm increased while the volume of particles smaller than 50 μm decreased. This trend was observed on further heating to 1150 °C. The mean particle sizes of lizardite heat-treated at 900 °C and 1150 °C were 34.8 μm and 142.1 μm, respectively (Table 2 and Fig. 5). These increases in the particle sizes correspond to the growth of denser phases such as $Al_{2.35}Si_{0.64}O_{4.82}$ (mullite), SiO_2 (cristobalite), Mg_2SiO_4 (forsterite), and $Fe_{0.3}Mg_{0.7}(SiO_3)$ (enstatite) on heating (Fig. 3). Further evidence of larger and well-defined particles in lizardite heat-treated to 900 °C and 1150 °C (Fig. 6(b) and (c)) were

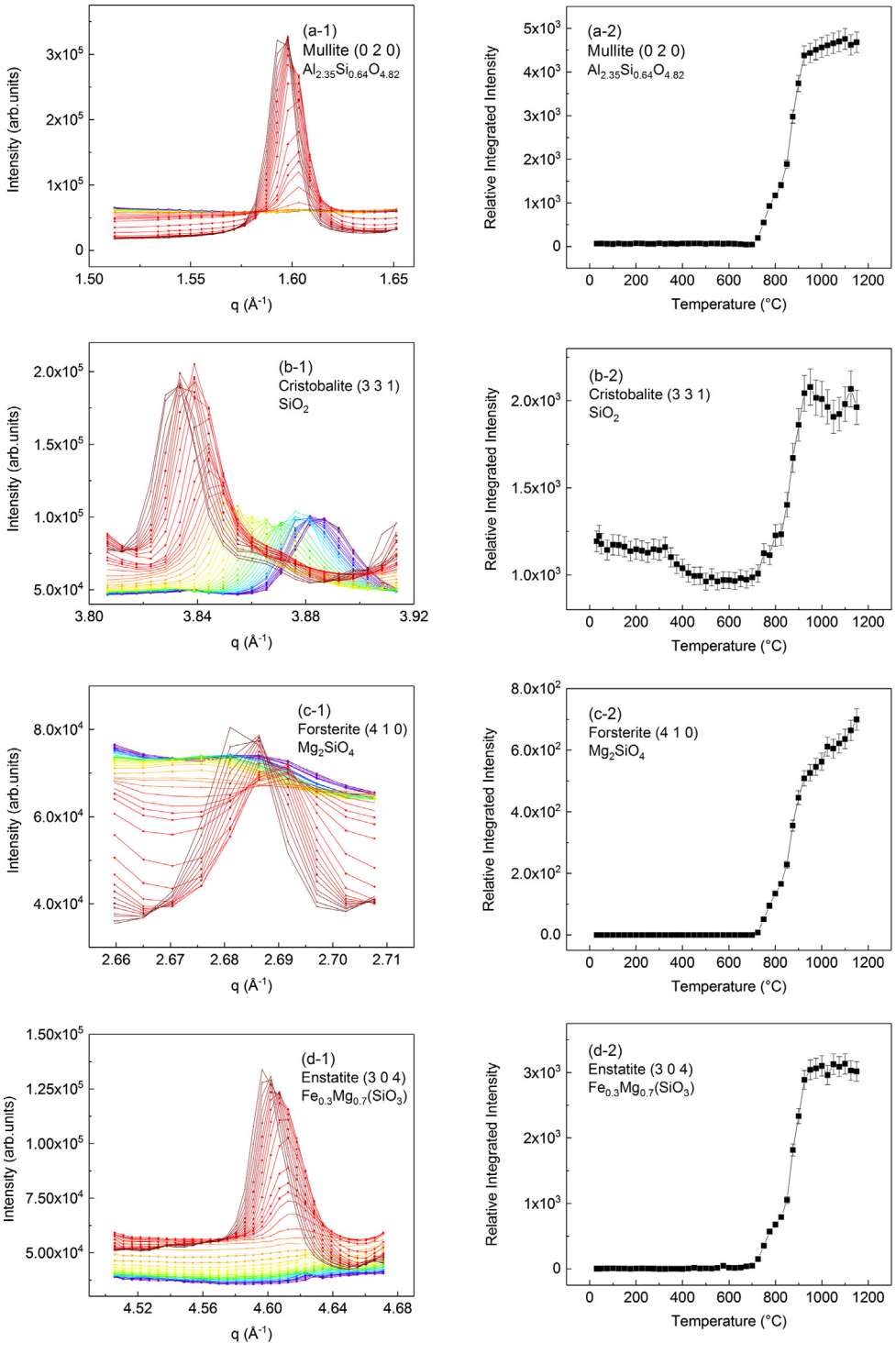

Fig. 3. Changes in the characteristic peaks of mullite (d = 3.84 Å, q = 1.59 Å^{-1}, hkl: (020)[32]) (a-1), cristobalite (d = 1.64 Å, q = 3.83 Å^{-1}, hkl: (331)[33]) (b-1), forsterite (d = 1.37 Å, q = 4.60 Å^{-1}, hkl: (304) [34]) (c-1), and enstatite (d = 1.37 Å, q = 4.60 Å^{-1}, hkl: (304)[35]) (d-1) on heating from 30 °C to 1150 °C. The corresponding integrated intensities of mullite (a-2), cristobalite (b-2), forsterite (c-2), and enstatite (d-2) show the onset of these phases at temperatures in the range of 725 °C and 750 °C. The relative integrated intensities represented in the right panel correspond to the integrated intensity of the characteristic peak at a given temperature normalized to the integrated intensity at 30 °C. Vertical bars in (a-2), (b-2), (c-2), and (d-2) represent estimated 5% standard deviation uncertainties.

noted compared to untreated lizardite (Fig. 6(a)).

The changes in the pore-solid interface and the morphological transformations of lizardite from a lamellar to a pseudo-amorphous to a crystalline structure are supported by USAXS and SAXS measurements (Fig. 7). At a high q of 0.85 Å^{-1}, the peak corresponding to the interlayer basal reflection was noted. Shifts in the peak position were not noted on heating to 800 °C suggesting that the d-spacing of 7.39 Å did not change on heating. Significant changes in the intensity of this peak

Table 2
Summary of the surface area, cumulative pore volume, and mean particle size of untreated serpentine at 25 °C and heat-treated at 350 °C, 650 °C, and 900 °C.

Sample Temperature (°C)	25	350	650	900	1150
Surface Area (m^2/g)	36.3 ± 9.5	580.4 ± 14.0	1152.0 ± 37.0	6.6 ± 0.2	–
Cumulative Pore Volume (cc/g)	0.11 ± 0.01	0.89 ± 0.01	1.56 ± 0.01	0.05 ± 0.01	–
Average Mean of Particle Size (μm)	10.8 ± 0.5	12.4 ± 0.8	13.1 ± 1.4	34.8 ± 2.4	142.1 ± 1.6

on heating were noted as shown in Fig. 1 and discussed in Section 3.1. A decrease in the nano-scale porosity corresponding to the reduction in the intensity of this basal peak was noted on heating above 550 °C. This peak completely disappears on heating to 825 °C.

It was interesting to note the growth of an additional feature in the q range of 0.45 $Å^{-1}$–0.70 $Å^{-1}$ on heating from 50 °C to 725 °C. This feature decreased in intensity on heating above 800 °C before disappearing. The growth of this feature corresponded to the reduction in the intensity of d (001) peak. McKelvy and co-workers referred to this feature as the α phase which reflects the diffuse interlamellar order in lizardite on heating [19]. Our results are consistent with their observations that heat treating serpentine to temperatures up to 800 °C results in the formation of pseudo-amorphous serpentine characterized by intralamellar disorder emerging from changes in the d (001) peak with the development of diffuse interlamellar order in q range of 0.45 $Å^{-1}$–0.70 $Å^{-1}$. This α feature disappears on heating above 800 °C which corresponds to the growth of dense crystalline phases (Fig. 3).

In addition to providing insights into the changes in the lamellar structure on heating, the combined USAXS/SAXS data yielded detailed information of the changes in the pore-solid interface. One approach to quantify the changes in the pore-solid interface is the Porod slope [41]. The Porod slope yields information about the "fractal dimension" of the scattering object. In this study, the Porod slope is calculated in the q region of 0.02–0.4 $Å^{-1}$ to probe the fractality of the local structure. The Porod slope is calculated using the following relationships where $I(q)$ and n represent the scattering intensity and the slope, respectively.

$$I(q) = \frac{A}{q^n} + B \tag{1}$$

$$\log_{10}[I(q) - B] = \log_{10}A - n\log_{10}q \tag{2}$$

Porod slopes of 1 or 4 represent scattering from rigid rods or smooth surfaces, respectively. Porod slopes between 3 and 4 represent rough interfaces with a fractal dimension, D where $n = 6 - D$ represents a surface fractal. A slope between 2 and 3 represents branched systems or networks also known as mass fractals. The Porod slopes of serpentine on heating from ambient temperature to 425 °C are in the range of 3.1 and 3.2 indicating a rough interface (Fig. 8). Further heating to 675 °C and 700 °C reduced the Porod slope to 3.0 and 2.8, respectively. The decreasing Porod slope is indicative of a branched network consistent with the formation of pseudo-amorphous structure at these temperatures. Further heating to 1150 °C increased the Porod slope to 3.7 indicating the formation of increasingly smoother interfaces which is consistent with the growth of various crystalline phases (Fig. 3). By combining *in-operando* USAXS/SAXS/WAXS measurements with complementary characterization tools, a detailed structural and morphological basis spanning from the angstrom – to – micrometer scale was established for the enhanced reactivity of serpentine heated to temperatures in the range of 600 °C–700 °C.

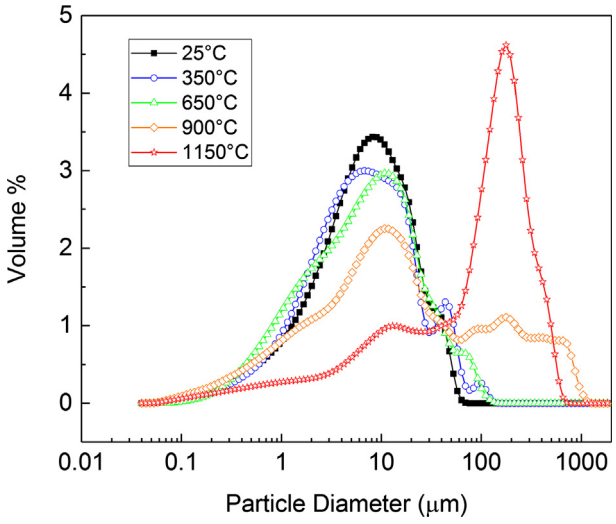

Fig. 5. Changes in the particle size distributions of lizardite heat treated at 350 °C, 650 °C, and 900 °C with respect to untreated lizardite at 25 °C.

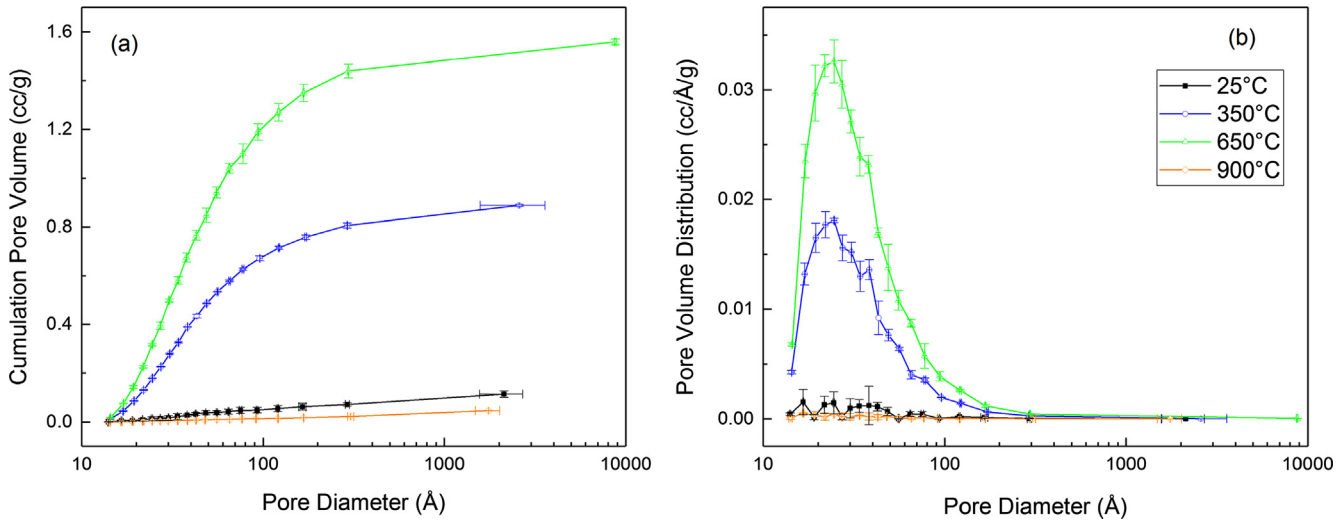

Fig. 4. Changes in the cumulative pore volume (a) and pore volume distributions (b) in lizardite heat treated at 350 °C, 650 °C, and 900 °C with respect to untreated lizardite at 25 °C.

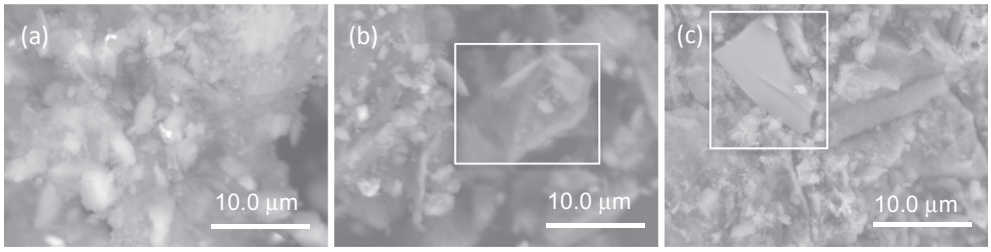

Fig. 6. Comparison of morphological changes of untreated lizardite at 25 °C (a) with lizardite heat-treated at 900 °C (b) and 1150 °C (c) using scanning electron microscopy images. The particles within the white square correspond to the crystalline phases formed at elevated temperatures.

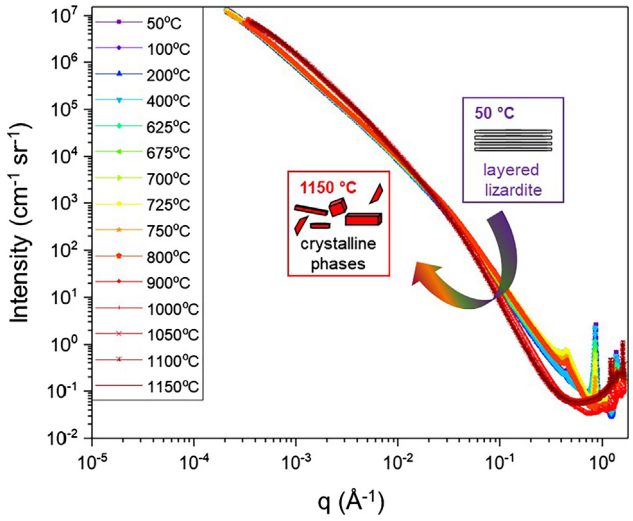

Fig. 7. Changes in the combined slit-smeared USAXS/SAXS data on heating lizardite to a nominal temperature of 1150 °C. An increase in the scattering intensity is noted on heating to 700 °C at q larger than 0.03 Å^{-1}. This transformation corresponds to the change in the lamellar morphology of lizardite at ambient temperature to a pseudo-amorphous structure. Further heating to 1150 °C results in the formation of crystalline phases (see Fig. 3) and is accompanied by a reduction in the scattering intensity at q larger than 0.03 Å^{-1}.

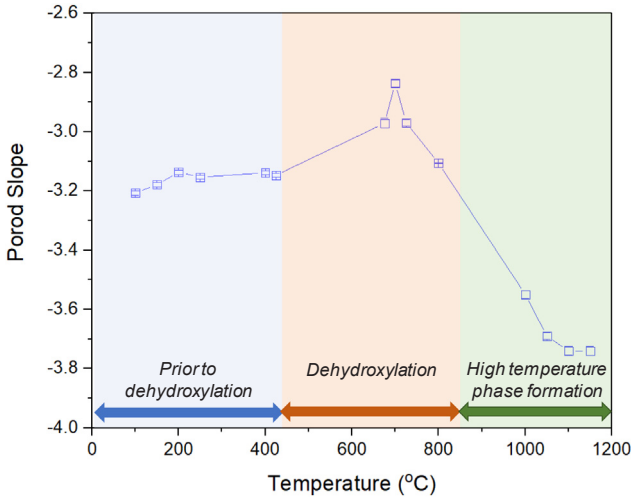

Fig. 8. Changes in Porod slopes for q in the range of 0.02 Å^{-1}–0.4 Å^{-1}. The slopes are determined after desmearing the USAXS/SAXS data shown in Fig. 7. The roughness of the pore-solid interfaces increases on serpentine dehydroxylation. These interfaces become smoother on the formation of high temperature phases such as $Al_{2.35}Si_{0.64}O_{4.82}$ (mullite), SiO_2 (cristobalite), Mg_2SiO_4 (forsterite), $Fe_{0.3}Mg_{0.7}(SiO_3)$ (enstatite).

4. Conclusions

In this study, the structural and morphological basis for the enhanced reactivity of serpentine heat-treated to temperatures in the range of 600 °C and 700 °C with CO_2 was evaluated. Heating serpentine to temperatures in the range of 600 °C and 700 °C resulted in the formation of a pseudo-amorphous serpentine structure which corresponded to a significant increase in the surface area and porosity on heating. These measurements provide a fundamental basis for reacting serpentine to temperatures in the range of 600 °C and 700 °C prior to accelerated conversion to carbonates. Further heating reduced the porosity and the reactive surface area of heat-treated serpentine which corresponded to the formation of high temperature crystalline phases such as $Al_{2.35}Si_{0.64}O_{4.82}$ (mullite), SiO_2 (cristobalite), Mg_2SiO_4 (forsterite), and $Fe_{0.3}Mg_{0.7}(SiO_3)$ (enstatite). Dynamic changes in the pore-solid interface determined using USAXS/SAXS measurements showed an increasing roughness leading to the formation of a branched network on heating serpentine to 700 °C. Further heating yielded smoother interfaces consistent with the formation of high temperature crystalline phases.

Acknowledgements

The authors gratefully acknowledge the Wisconsin Alumni Research Foundation and the College of Engineering at the University of Wisconsin, Madison. A special thanks to Dr. Jan Ilavsky and Dr. Ivan Kuzmenko, X-ray Science Division, Argonne National Laboratory, for providing experimental support for the combined USAXS/SAXS/WAXS measurements at the Advanced Photon Source. The use of the Advanced Photon Source, an Office of Science User Facility operated for the U.S. Department of Energy (DOE) Office of Science by Argonne National Laboratory, is supported by the U.S. DOE under Contract DE-AC02-06CH11357.

Appendix A. Supplementary data

Supplementary data associated with this article can be found, in the online version, at http://dx.doi.org/10.1016/j.fuel.2018.04.097.

References

[1] Lackner KS. Carbonate chemistry for sequestering fossil carbon. Annu Rev Energy Environ 2002;27:193–232.
[2] Gadikota G, Swanson EJ, Zhao H, Park A-HA. Experimental design and data analysis for accurate estimation of reaction kinetics and conversion for carbon mineralization. Ind Eng Chem Res 2014;53:6664–76.
[3] Gadikota G, Matter J, Kelemen P, Park A-HA. Chemical and morphological changes during olivine carbonation for CO_2 storage in the presence of NaCl and $NaHCO_3$. PCCP 2014;16:4679–93.
[4] Park A-HA, Fan L-S. CO_2 mineral sequestration: physically activated dissolution of serpentine and pH swing process. Chem Eng Sci 2004;59:5241–7.
[5] Béarat H, McKelvy MJ, Chizmeshya AVG, Gormley D, Nunez R, Carpenter RW, et al. Carbon sequestration via aqueous olivine mineral carbonation: role of passivating layer formation. Environ Sci Technol 2006;40:4802–8.
[6] Chizmeshya AVG, McKelvy MJ, Squires K, Carpenter RW, Béarat H. A novel approach to mineral carbonation: Enhancing carbonation while avoiding mineral pretreatment process cost: DOE Final Report 924162; 2007.

[7] Gadikota G, Park A-HA. Accelerated carbonation of Ca- and Mg-bearing minerals and industrial wastes using CO_2, in carbon dioxide utilization; 2014.
[8] Li J, Hitch M. Structural and chemical changes in mine waste mechanically-activated in various milling environments. Powder Technol 2017;308:13–9.
[9] Power IM, Harrison AL, Dipple GM, Wilson SA, Kelemen PB, Hitch M, et al. Carbon mineralization: from natural analogues to engineered systems. Rev Min Geochem 2013;77:305–60.
[10] Ryu KW, Jo H, Choi SH, Chae SC, Jang YN. Changes in mineral assemblages during serpentine carbonation. Appl Clay Sci 2016;134:62–7.
[11] Farhang F, Oliver TK, Rayson M, Brent G, Stockenhuber M, Kennedy E. Experimental study on the precipitation of magnesite from thermally activated serpentine for CO_2 sequestration. Chem Eng J 2016;303:439–49.
[12] Werner M, Hariharan S, Mazzotti M. Flue gas CO_2 mineralization using thermally activated serpentine: from single-to double-step carbonation. PCCP 2014;16:24978–93.
[13] Park A-HA, Jadhav R, Fan L. CO2 mineral sequestration: chemically enhanced aqueous carbonation of serpentine. Can J Chem Eng 2003;81:885–90.
[14] Wilson SA, Raudsepp M, Dipple GM. Verifying and quantifying carbon fixation in minerals from serpentine-rich mine tailings using the Rietveld method with X-ray powder diffraction data. Am Mineral 2006;91:1331–41.
[15] Highfield J, Lim H, Fagerlund J, Zevenhoven R. Activation of serpentine for CO_2 mineralization by flux extraction of soluble magnesium salts using ammonium sulfate. RSC Adv 2012;2:6535–41.
[16] Barnes VE, Shock DA, Cunningham WA. Utilization of texas serpentine; 1950.
[17] Gerdemann SJ, O'Connor WK, Dahlin DC, Penner LR, Rush H. Ex situ aqueous mineral carbonation. Environ Sci Technol 2007;41:2587–93.
[18] Werner M, Hariharan S, Mazzotti M. Flue gas CO_2 mineralization using thermally activated serpentine: from single- to double-step carbonation. PCCP 2014;16:24978–93.
[19] McKelvy MJ, Chizmeshya AVG, Diefenbacher J, Béarat H, Wolf G. Exploration of the role of heat activation in enhancing serpentine carbon sequestration reactions. Environ Sci Technol 2004;38:6897–903.
[20] Gadikota G, Allen AJ. Microstructural and structural characterization of materials for CO_2 storage using multi-scale X-ray scattering methods. In: Li L, Wong-Ng W, editors. Mater. Process. CO_2 capture, conversion, sequestration. Wiley Books; 2018.
[21] Gadikota G. Connecting the morphological and crystal structural changes during the conversion of lithium hydroxide monohydrate to lithium carbonate using multi-scale X-ray scattering measurements. Minerals 2017;7:169.
[22] Gadikota G, Zhang F, Allen AJ. In situ angstrom-to-micrometer characterization of the structural and microstructural changes in kaolinite on heating using ultrasmall-angle, small-angle, and wide-angle X-ray acattering (USAXS/SAXS/WAXS). Ind Eng Chem Res 2017;11791–11801.
[23] Gadikota G, Zhang F, Allen AJ. Towards understanding the microstructural and structural changes in natural hierarchical materials for energy recovery: in-operando multi-scale X-ray scattering characterization of Na- and Ca-montmorillonite on heating to 1150 C. Fuel 2017;196:195–209.
[24] Rucklidge JC, Zussman J. The crystal structure of the serpentine mineral, lizardite $Mg_3Si_2O_5(OH)_4$. Acta Crystallogr. 1965;19:381–9.
[25] Bonse U, Hart M. Tailless x-ray single-crystal reflection curves obtained by multiple reflection. Appl Phys Lett 1965;7:238–40.
[26] Ilavsky J, Jemian PR, Allen AJ, Zhang F, Levine LE, Long GG. Ultra-small-angle X-ray scattering at the advanced photon source. J Appl Crystallogr 2009;42:469–79.
[27] Ilavsky J, Jemian PR. Irena: tool suite for modeling and analysis of small-angle scattering. J Appl Crystallogr 2009;42:347–53.
[28] Ilavsky J. Nika: software for two-dimensional data reduction. J Appl Crystallogr 2012;45:324–8.
[29] Ferrage E, Lanson B, Malikova N, Plançon A, Sakharov BA, Drits VA. New insights on the distribution of interlayer water in bi-hydrated smectite from X-ray diffraction profile modeling of 00l reflections. Chem Mater 2005;17:3499–512.
[30] Ferrage E, Kirk CA, Cressey G, Cuadros J. Dehydration of Ca-montmorillonite at the crystal scale. Part I: Structure evolution. Am Mineral 2007;92:994–1006.
[31] Trittschack R, Grobéty B. Dehydroxylation kinetics of lizardite. Eur J Mineral 2012;24:47–57.
[32] Angel RJ, Prewitt CT. Crystal structure of mullite: a re-examination of the average structure. Am Mineral 1986;71:1476–82.
[33] Dove MT, Craig MS, Keen DA, Marshall WG, Redfern SAT, Trachenko K, et al. Crystal structure of the high-pressure monoclinic phase-II of cristobalite, SiO_2. Mineral Mag 2000;64:569–76.
[34] Hazen RM. Effects of temperature and pressure on the crystal structure of forsterite. Am Mineral 1976;61:1280–93.
[35] Smith JV. The crystal structure of proto-enstatite, $MgSiO_3$. Acta Crystallogr 1959;12:515–9.
[36] Ismail MGMU, Nakai Z, Sōmiya S. Microstructure and mechanical properties of mullite prepared by the sol-gel method. J Am Ceram Soc 1987;70.
[37] Barzegar Bafrooei H, Ebadzadeh T, Majidian H. Microwave synthesis and sintering of forsterite nanopowder produced by high energy ball milling. Ceram Int 2014;40:2869–76.
[38] Downs RT, Palmer DC. The pressure behavior of alpha cristobalite. Am Mineral 1994;79:9–14.
[39] Ahrens TJ, Gaffney ES. Dynamic compression of enstatite. J Geophys Res 1971;76:5504–13.
[40] Viti C, Hirose T. Thermal decomposition of serpentine during coseismic faulting: nanostructures and mineral reactions. J Struct Geol 2010;32:1476–84.
[41] Porod G. X-ray low angle scattering of dense colloid systems, part I. Kolloid Z 1951;124:83–114.
[42] Mellini M. The crystal structure of lizardite 1T: hydrogen bonds and polytypism. Am Mineral 1982;67:587–98.